



High-Efficiency Photodetectors Based on Zinc Oxide Nanostructures on Porous Silicon Grown by Pulsed Laser Deposition

Ali J. Hadi¹ · Uday M. Nayef¹ · Falah A.-H. Mutlak² · Majid S. Jabir¹

Received: 4 August 2023 / Accepted: 22 August 2023 / Published online: 30 August 2023
© The Author(s), under exclusive licence to Springer Science+Business Media, LLC, part of Springer Nature 2023

Abstract

In this study deposited zinc oxide (ZnO) nanostructures were prepared by pulsed laser deposition (PLD) technique on porous silicon (PS) substrates that were prepared via photoelectrochemical etching of silicon n-type (100). The study investigated the influence of laser energy on various characteristics of the fabricated devices, including their optical, morphological, structural, electrical, and photodetector features. The X-ray diffraction results indicate a dominant broad diffraction peak at 69.14° , and the ZnO phase aligns with the hexagonal wurtzite structure. The field emission scanning electron microscopy micrograph illustrates that porous silicon has a sponge-like fashion, while ZnO nanostructures have spherical grains distributed randomly and grow larger with laser energy. The optical characteristics of the manufactured samples were examined using techniques that include UV–vis absorption spectroscopy, UV–vis diffuse reflectance spectrometry, and photoluminescence spectroscopy. The findings indicated that decreased laser energy led to a blue shift in the energy gap. The reflectivity of the produced samples decreased after the deposition of a zinc oxide layer over porous silicon. The photoluminescence examination showed the presence of four distinct emission peaks, namely, UV, violet-blue, blue, and green, consequent to coating a ZnO layer onto the porous silicon substrate. Fourier transform infrared spectroscopy confirmed that ZnO thin films deposited on porous silicon cause surface oxidation and produced a new peak at 455.2 cm^{-1} related to the Zn–O stretching band. The current density–voltage properties of the fabricated devices in the absence and presence of white light were investigated as a function of laser energy. The ZnO NPs/PS/n-Si photoreactors displayed rectifier features and had outstanding spectral responsivity from ultraviolet to near-infrared. Moreover, the fabricated photoreactor showed the most prominent external quantum efficiency (EQE) in the UV region. The results of this study are of great importance to the advancement of photodetectors and optoelectronic devices based on ZnO and porous silicon.

Keywords ZnO nanostructure · Pulse laser deposition · Optical properties · Electrical properties · Photodetector

Introduction

Nanostructure materials have attracted the interest of scientists in recent years by producing and enhancing advanced materials with significant physical and chemical properties to improve optoelectronic devices [1–3]. The use of transparent conductive oxide (TCO) films has garnered considerable attention in recent times owing to its extensive range of applications in optoelectronic devices, including

liquid crystal displays, flat panel displays, thin film photovoltaic cells, transparent thin film transistors, and light emitting diodes [4, 5]. Among these oxide materials, zinc oxide (ZnO) is a typical n-type II–IV semiconductor and an appropriate selection based on its broad direct band gap of 3.37 eV, great exciton binding energy of 60 meV, as well as prominent electron mobility. In addition, these materials' distinct electrical and optical characteristics, relatively inexpensive, lack of toxicity, and relatively low deposition temperature are crucial for developing solar cells, sensors, and photodetector technologies [6–8].

Different techniques have been carried out to the coating of ZnO layer PS, including chemical spray pyrolysis, the sol–gel process [9], chemically vaporized deposition (CVD), radio-frequency magnetron sputtering, molecular beam epitaxy, solid-state chemical reactions, and PLD

✉ Uday M. Nayef
uday.nayef@uotechnology.edu.iq

¹ Department of Applied Science, University of Technology, Baghdad, Iraq

² College of Science, University of Baghdad, Baghdad, Iraq

[10–12]. PLD has numerous benefits over alternative techniques, including one-step production, simple operation, rapid reactive processes, absence of component differences, and production of high-quality films at lower substrate temperatures [13]. In reality, the drop in deposition temperature in the PLD process is compensated by the high energy of the ablated fragments in the laser-generated plasma plume. This versatile technique provides controllable thickness, stoichiometry, and composition, making it an excellent method for synthesizing thin films with superior structural and optical properties [14, 15]. Deposition parameters such as laser energy, target-substrate separation, substrate temperature, and relative oxygen pressure affect PLD-grown ZnO thin coatings [16].

In addition, selecting the type of substrate for the deposition of thin ZnO layers is crucial for improving physical, optical, and electrical properties. The growth and analysis of the ZnO layers grown on various substrates, including glass, metallic substrates, ITO, FTO, and silicon substrates, have been extensively investigated [17]. Despite the fact that the growth of a ZnO thin film on a silicon substrate may lead to increased mechanical stress between the ZnO and Si substrate owing to significant variations in lattice constant and thermal expansion coefficient, thus, mechanical stress can be minimized by manipulating the Si surface [18].

A straightforward method for redesigning silicon's surface is to produce porous silicon by electrochemically etching silicon samples [19, 20]. Porous silicon exhibits a sponge-like structure and a high ratio of surface area to volume, which makes distinct physical properties compared to bulk silicon, such as a more significant energy gap and a lower refractive index than crystalline silicon [21]. The porosity reduces the mismatch in lattice and thermal expansion coefficient disparity between silicon and zinc oxide. It provides an appropriate base for accepting zinc oxide within their pores and is extremely attractive for optical applications, including UV detection [11]. In addition, porous silicon has been reported to enhance the photoluminescence of zinc oxide at ambient temperature [22].

There is limited literature available on the physical, electrical, and optical features of ZnO produced on porous silicon using the PLD technique. Wang et al. [23] produced ZnS and ZnO films via pulsed laser deposition on porous silicon substrates and found surface cracks in the obtained sample. Abood et al. [24] achieved enhanced solar cell efficiency by utilizing the PLD method to deposit a hexagonal crystalline film on porous silicon. The resulting film exhibited high UV absorption, a grain size of 17.5 nm, and a wide bandgap of 3.7 eV. However, many papers have reported on photodetectors' fabrication, characterization, and efficiency analysis utilizing a ZnO/PS device, whereas different methods used the ZnO layer on porous silicon. Shabannia et al. [3] employed chemical bath deposition to synthesize ZnO

nanorods on a porous silicon substrate. They observed that the resulting photodetector demonstrated favorable structural and optical characteristics with a responsivity magnitude of 1.738 A/W. Abed et al. [25] compared RF-sputtering and drop-casting methods for fabricating photodetectors using zinc oxide nanorods seeded onto porous silicon. They discovered that drop-casting photodetectors show the best electrical efficiency, and the device has a responsivity magnitude of 1.12 A/W.

In this study, we provide findings about the influence of laser energy in the PLD technique on physical properties and the efficiency of photodetectors composed of ZnO nanostructure embedded in porous silicon without post-annealing.

Materials and Methods

In this study, the photoelectrochemical etching of a single-crystal silicon wafer was the basis for preparing porous silicon. The starting material was an n-type silicon wafer with a crystallographic orientation (100), single-sided polishing, a resistivity range of 1–10 $\Omega\cdot\text{cm}$, and a thickness of $575 \pm 25 \mu\text{m}$. An ohmic contact was created by coating an n-type Si wafer's unpolished side with an aluminum layer. A diamond saw cuts the silicon wafer with a $1.5 \times 2.5 \text{ cm}$ dimension. The sample was cleansed with absolute ethanol and then rinsed with distilled water for 8 min to eliminate residual contaminants. The silicon slice was then desiccated with a stream of dry air. A silicon piece was inserted through an O-ring rubber so that only the front side was exposed to the electrolyte solution through the etching process. Rubber O-rings were utilized to prevent solution leakage, and a stainless steel foil was attached to the substrate's back face to ensure excellent electrical contact. The photoelectrochemical etching was achieved in a two-electrode cell using a gold electrode as a cathode and the prepared silicon slice as an anode. Two electrodes were used to apply current across the anodization cell. The anodization cell was constructed from Teflon to prevent interaction with HF acid. The cell had a 1 cm^2 central circular opening for contacting the silicon wafer. The silicon sample was subjected to a current density of 16 mA/cm^2 for 10 min at room temperature under the illumination of a tungsten lamp (200 W) to create a porous structure. This was achieved by immersing the sample in an electrolyte containing 48% hydrofluoric acid (HF) and 99.99% absolute ethanol ($\text{C}_2\text{H}_5\text{OH}$) with a volumetric ratio 1:2. Ethanol served as a surfactant to reduce hydrogen bubbles on the top surface of the silicon. Following the anodization process, the sample was cleaned with absolute ethanol and dried gently with dry air.

The present study investigated the deposition of a ZnO thin layer on two substrates using pulsed laser deposition. The substrates were porous silicon and quartz, which were placed inside the pulsed laser deposition system and maintained at a vacuum pressure of 5×10^{-2} mbar. The separation between the zinc metal pellet and the substrates was determined to be 11 cm.

A high-purity zinc powder (99.8% purity) was pressed to form a zinc metal target measuring $2 \text{ cm} \times 2 \text{ cm} \times 0.2 \text{ cm}$. The target was then ablated using a Q-switched Nd:YAG pulsed laser with the following parameters: 1064 nm wavelength, 10 ns pulse duration, and 1 Hz repetition rate. The laser energy was varied from 400 to 800 mJ/pulse for 300 laser pulses to achieve sufficient laser fluence, estimated at 1.5 mm spot size using a 110 mm focal length plano-convex lens focused on the zinc target. The incident angle of the laser beam onto the zinc (Zn) target was fixed at 45° . The ZnO thin film deposition occurred at room temperature. The schematic diagram for depositing the ZnO layer on porous silicon substrate is depicted in Fig. 1.

To examine the electrical and photodetector characteristics of the ZnO NPs/PS sandwich structure, a layer of ZnO was coated with an aluminum contact with a thickness of approximately 320 nm using the thermal evaporation technique. The aluminum layer was deposited under a 2×10^{-6} mbar pressure.

Characterization Techniques

The produced samples were characterized using several analytical techniques. The morphologies of the PS structure and ZnO NPs/PS layers were examined using an FEI INSPECT model F50 field emission scanning electron microscope (FE-SEM). The structural properties of the ZnO NPs/PS sandwich structure were investigated using an X-ray diffraction pattern with $\text{CuK}\alpha$ radiation at 1.54060 \AA and running at 40 kV and 30 mA. The analysis was conducted in the 2θ range of $20\text{--}80^\circ$ using a Shimadzu Company X-ray diffraction instrument. The optical characteristics of ZnO NPs were recorded via UV–Vis absorption spectroscopy with a spectroscopic system from the Perkin Elmer Company and a wavelength range of 240–800 nm. Additionally, the reflectance of the ZnO NPs/PS device was measured using a UV–Vis diffuse reflectance spectrometer with a wavelength range of 240–1000 nm from the Avantes DH-S-BAL-24048 UV–Vis, the Netherlands. The PL spectroscopic analysis was conducted at room temperature using a FluoroMate Fs-2 spectrometer with an excitation wavelength of 325 nm and recorded emission spectra between 350 and 800 nm wavelengths. The electrical measurements of Al/ZnO NPs/PS/n-Si/Al photodetector were assessed in the dark with forward and reverse biasing and illumination with reverse biasing using tungsten lamps 200 W set at $20\text{--}180 \text{ mW/cm}^2$ light

Fig. 1 A schematic illustration of the pulse laser deposition (PLD) system

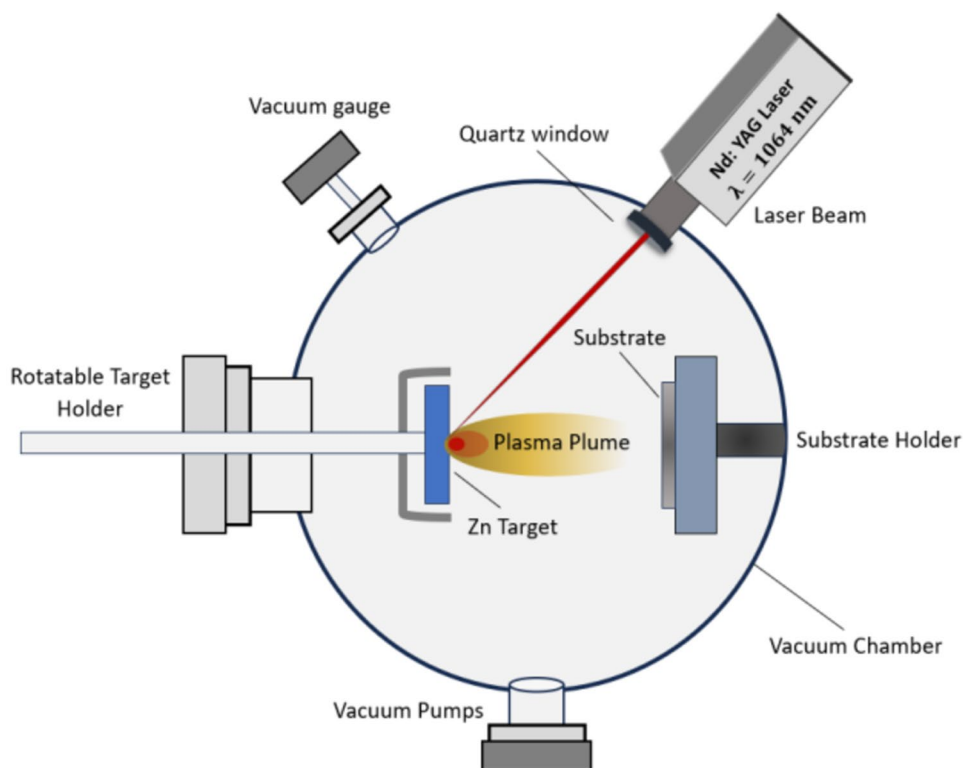
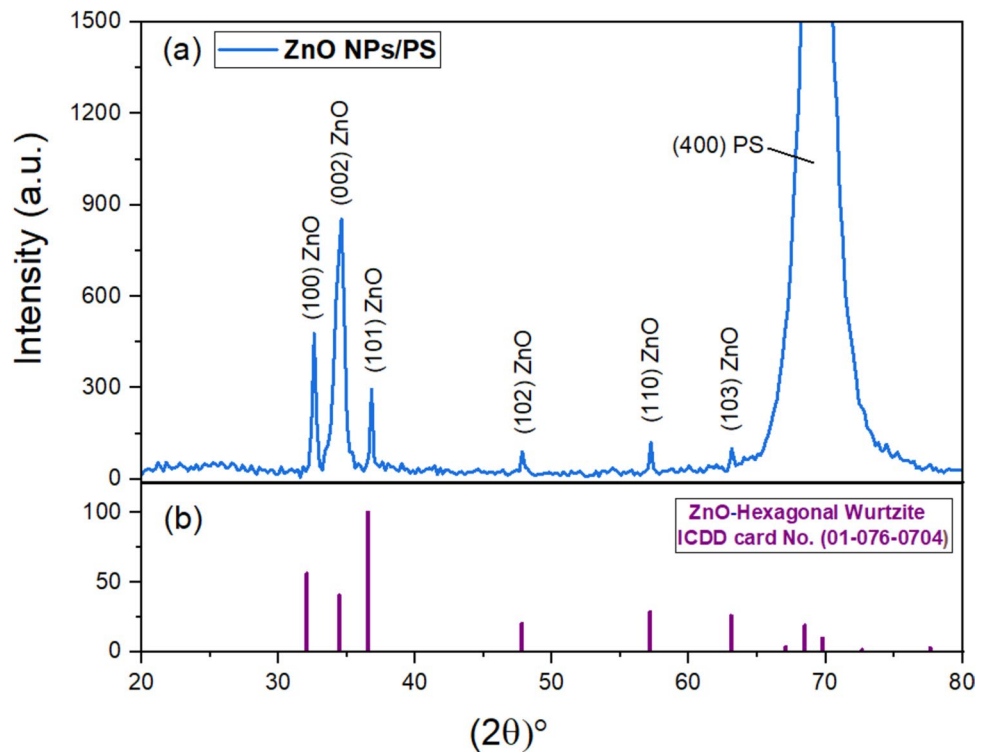


Fig. 2 a The XRD analysis of prepared ZnO NPs using the PLD technique at 800 mJ laser energy and deposited on porous silicon fabricated at 16 mA/cm² for 10 min. **b** Standard diffraction pattern of hexagonal wurtzite (JCPDS code No. #01–076-0704)



densities. The photocurrent of the device was recorded using a 100 W tungsten light as the illumination source, and the power of the radiation was calibrated using a silicon power meter before the measurement. The spectral responsivity of the sandwich structure photodetector was determined in the spectral range of 300–900 nm using a monochromator.

Results and Discussion

Structural Analysis and Particle Size

X-ray analysis was carried out to obtain information about the sample structure and phase. Figure 2(a) displays the XRD spectrum of the ZnO layer synthesis by pulsed laser deposition at 800 mJ laser energy and coated on a porous

silicon substrate obtained by photoelectrochemical etching at 16 mA/cm² through 10 min. Figure 2(a) exhibited a dominant broad diffraction peak at $2\theta = 69.14^\circ$, corresponding to (400) reflection of the PS substrate, in agreement with cubic silicon standard card (JCPDS card No. #027–1402) [26, 27]. Moreover, there are six diffraction peaks at $2\theta = 32.56^\circ, 34.59^\circ, 36.49^\circ, 47.87^\circ, 57.16^\circ,$ and 63.18° , which align with the (100), (002), (101), (102), (110), and (103) crystal planes, respectively. Upon contrasting these peaks, it can be observed that there is a preference for orientation along the (200) plane. These peaks matched the hexagonal wurtzite structure of the ZnO phase (JCPDS code No. #01–076-0704) [9], as described in Fig. 2(b). The apparent existence of both Si and ZnO nanocrystal diffraction peaks in Fig. 2(a) indicates that ZnO nanostructure integrated into the porous structure of PS.

Table 1 X-ray parameters of ZnO NPs/PS

Sample	Position JCPDS card no.	Position (2θ) (experimentally)	Orientation (hkl)	FWHM (degree)	Grain size (d) (nm)	Crystal structure type
ZnO NPs/PS	31.737	32.5626	(100)	0.61	13.57	Hexagonal wurtzite
	34.379	34.5883	(002)	0.52	16.03	Hexagonal wurtzite
	36.215	36.4937	(101)	0.48	17.43	Hexagonal wurtzite
	47.484	47.8705	(102)	0.96	9.05	Hexagonal wurtzite
	56.536	57.1641	(110)	0.48	18.85	Hexagonal wurtzite
	62.777	63.1806	(103)	0.63	14.80	Hexagonal wurtzite
	69.132	69.1428	(400)	0.72	13.40	Cubic

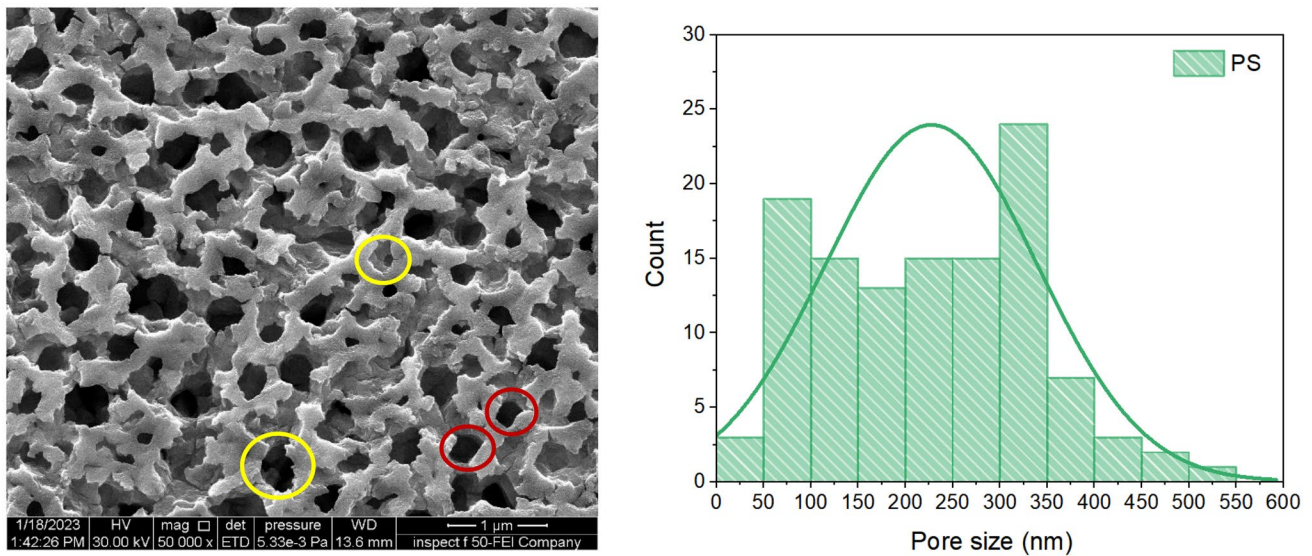


Fig. 3 FE-SEM micrograph of porous silicon structure grown on n (100) Si using photoelectrochemical etching method at a 16 mA/cm² current density for 10 min in 24% HF electrolyte solution

Table 1 presents the grain size (d) of the ZnO NPs and PS, which was determined using Debye–Scherrer’s relation and full width at half maximum (FWHM) of the X-ray peaks. Debye–Scherrer’s formula is expressed as follows [28]:

$$d = \frac{0.89 \lambda}{\beta \cos \theta} \quad (1)$$

where d represents the nanocrystallite size in nm, 0.89 is the Scherrer constant, λ is the X-ray wavelength in nm, and θ is the Bragg angle.

The crystallite size of ZnO NPs was calculated at the highest intensity to be 16.03 nm at (200) peak intensity. The XRD patterns did not indicate any subordinate or contaminant phase development. Hence, it may be noticed that the porous structure did not influence the hexagonal form of the wurtzite structure. Table 1 shows that the XRD peaks of ZnO have shifted toward higher diffraction angles, possibly due to porous silicon’s roughness and structural characteristics [11].

Morphological Analysis

The surface morphology properties of porous silicon and ZnO NPs/PS were investigated using field emission scanning electron microscopy (FE-SEM) analysis. Figure 3 displays a top layer image from FE-SEM of silicon produced through the photoelectrochemical anodization process of the n (100) silicon wafer at a current density of 16 mA/cm² for 10 min in 24% HF electrolyte solution. The FE-SEM image of the top view of the porous silicon depicts two separate sections: one with discrete pores with smooth walls and short branches

and the other with discrete pores resembling pits. The pores are a square-like shape and irregularly distributed on the surface, as illustrated by the red circle region in Fig. 3, with their square-like form attributable to the crystal’s face n-type (100) [29]. The average pore size of porous silicon was approximately 220 nm. The morphology of the porous silicon appears a sponge-like structure with micron-sized pores, consistent with the macroporous category [30, 31]. In addition to the pores on the surface, further pores developed a little below the surface, as shown by the regions marked with yellow circles in Fig. 3. This phenomenon’s cause is poorly understood. Even so, the occurrence of these subsurface pores can minimize the homogeneity and symmetry of the pore formation.

Figure 4 depicts FE-SEM micrographs of the ZnO layer deposited on porous silicon via PLD at room temperature at various laser energies (400–800 mJ/pulse). The FESEM images revealed that the ZnO NPs were spherical grains of various sizes and distributed randomly onto the PS surface. As shown in Fig. 4(a and b), the ZnO layer is partially filled across the pores of the PS structure after PLD treatment. In contrast, Fig. 4(c) images demonstrated that the zinc layers completely covered the surface of the porous silicon. The surface nanostructure of the ZnO layer in Fig. (4) revealed that the prepared samples’ morphology and average grain size depended on the laser energy used during deposition. The average grain size of the ZnO films deposited at 400 mJ/pulse laser energy was approximately 52 nm. At higher laser energies, the grain size of the ZnO layer increased, with a grain size of about 84 nm at 600 mJ laser energy and 97 nm at 800 mJ laser energy. The mean grain size of the ZnO

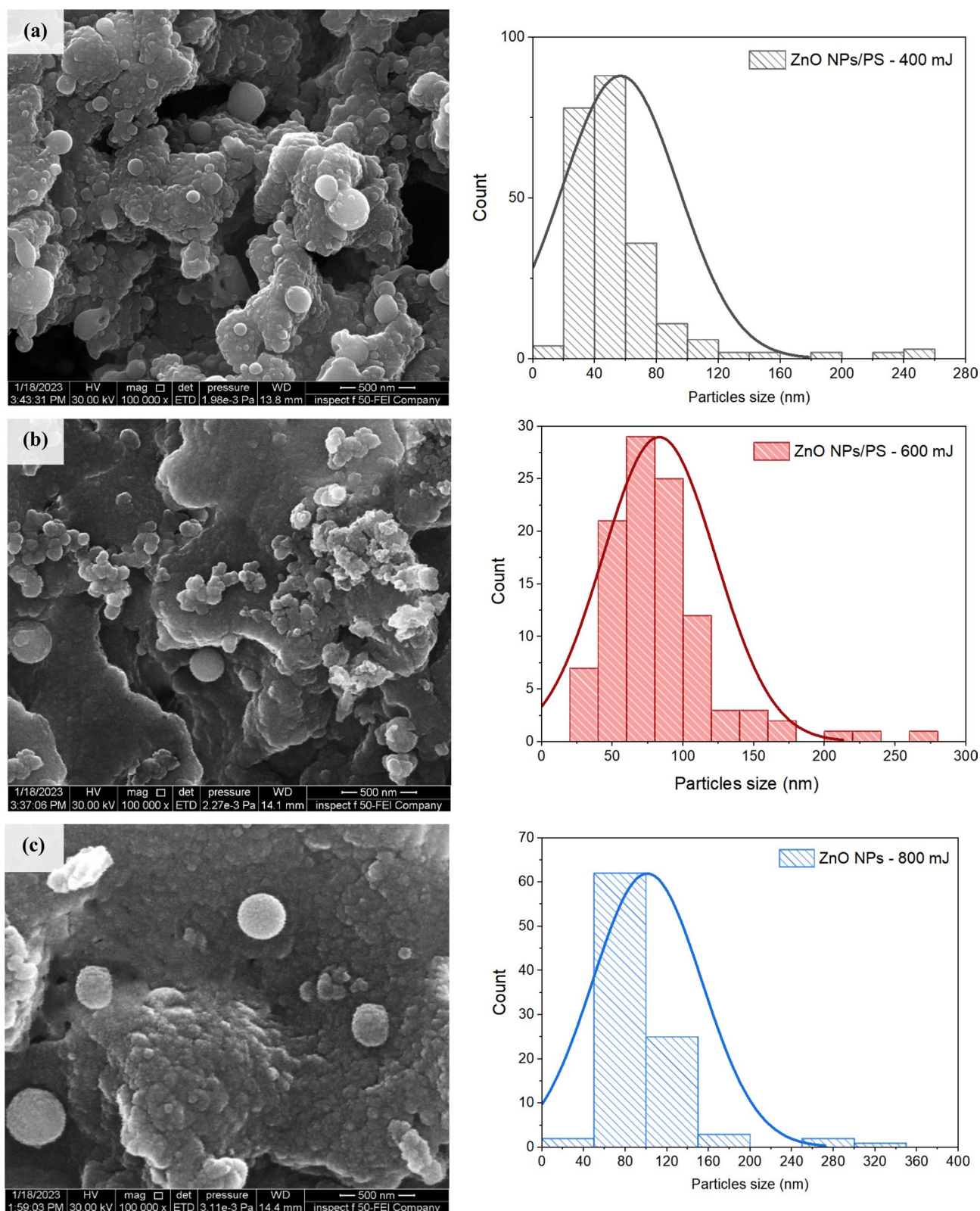


Fig. 4 FE-SEM micrograph of ZnO layer coated on porous silicon via pulsed laser deposition (PLD) at a various laser energies of **a** 400 mJ, **b** 600 mJ, and **c** 800 mJ for 300 pulses and wavelength of 1064 nm

nanostructure raised with more significant laser energy from 400 to 800 mJ/pulse in the PLD technique. The increase in grain size of ZnO nanostructures is attributable to the higher kinetic energy of ZnO atoms during deposition, which results in more efficient coalescence and development of the ZnO thin film. However, the ZnO nanostructure exhibited grain agglomeration at different laser energies on the PS surface, forming larger clusters. This behavior can be referred to the increased surface mobility of the ZnO particles, which promotes their adhesion and coalescence [32, 33]. The grain size estimated by Scherrer’s formula for a ZnO layer generated by PLD at 800 mJ laser energy resulted in 16.03 nm. However, FE-SEM analysis of the same parameter identified a particle size of approximately 97 nm. The distinction between XRD and FE-SEM, grain size measurements, was predicted because FE-SEM shows the grains without considering the presence of structural defects. In contrast, XRD determines the extent of the defect-free quantity.

Optical Properties

UV–Vis Absorption Spectroscopy

The optical absorption spectra in the wavelength range 240–800 nm of ZnO thin films deposited on quartz substrates using pulsed laser deposition at various laser energies are depicted in Fig. 5(a). The absorption spectrum of ZnO films deposited at room temperature exhibits significant UV features and a prominent absorption edge and tail bending, regardless of laser fluence. The absorption spectrum resembles spectra acquired by Ansari et al. [34] for ZnO thin film. An absorption peak was detected in each sample, ranging from 278 to 292 nm. This absorption peak is attributed to a

characteristic band for bulk ZnO [35]. The optical absorption of the film was found to increase with higher laser energy which may be ascribed to the increase in surface roughness and thickness of the film as the laser energy density is increased [10, 36, 37]. Furthermore, the synthesized ZnO thin films exhibited relatively low absorbance in both the visible and near-infrared spectral ranges. The high absorption in ZnO thin films at wavelengths below approximately 390 nm can be ascribed to the absorption of photons with energies greater than the optical energy band gap of the material. The absorption characteristics of the ZnO thin films were identified to be dependent on the laser energy used during deposition. Specifically, the sample fabricated at a laser energy of 800 mJ exhibited an absorption band with a peak at 291.9 nm and a significant broadening. As the laser energy was decreased, the main absorption band showed a blue shift, reduced broadening, and weakened absorption. For instance, in the sample prepared at a laser fluence of 400 mJ, the blue-shifted peak was observed at 278.2 nm with reduced broadening. It is noticed that absorption is shifted toward a lower wavelength (blue shift), and a decrease in peak width of the absorption band can be due to the reduction in mean grain size and the increase in bandgap that occur with increasing laser energy.

The optical band gap energy is an essential characteristic of semiconductors to define the optical and electronic properties. In the case of ZnO thin films, the direct band gap energy E_g can be computed by evaluating the absorption coefficient of the thin films as a function of photon energy. Namely, the relationship between the absorption coefficient and photon energy can be determined using the Tauc law (Eq. 2) [38]:

$$(ahv)^2 = A(hv - E_g) \tag{2}$$

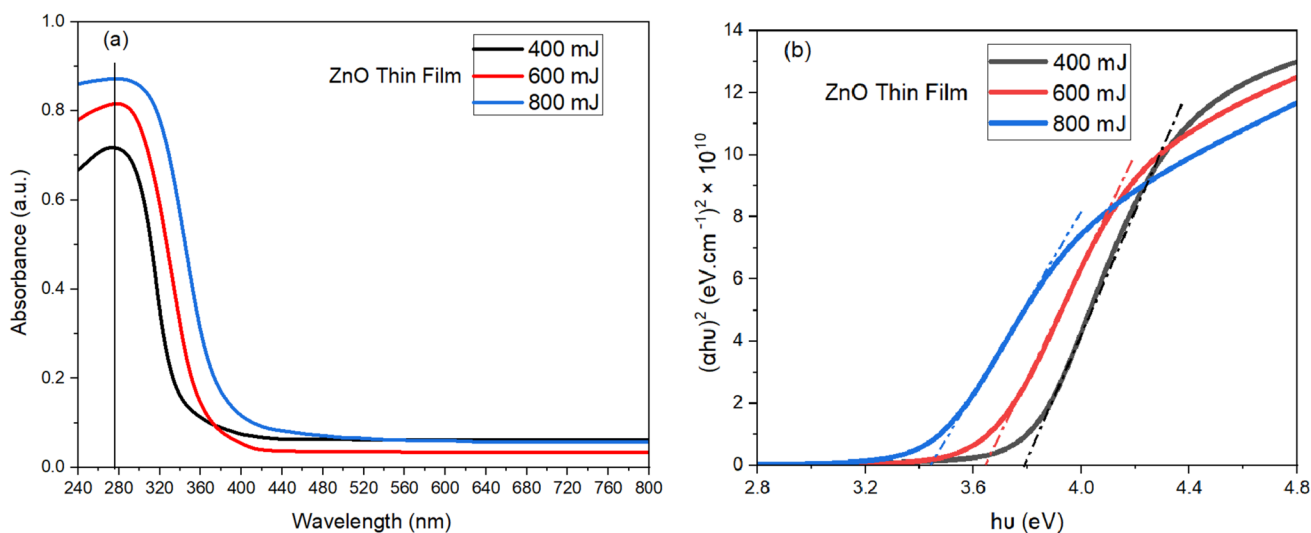


Fig. 5 **a** UV–vis spectra of ZnO layer deposited on quartz substrate using pulsed laser deposition method at laser energy. **b** The graph depicts plotting $(ahv)^2$ against the photon energy of ZnO thin films with different laser energies

Table 2 The absorption peak and band gap energy of obtained ZnO thin film versus different laser energies

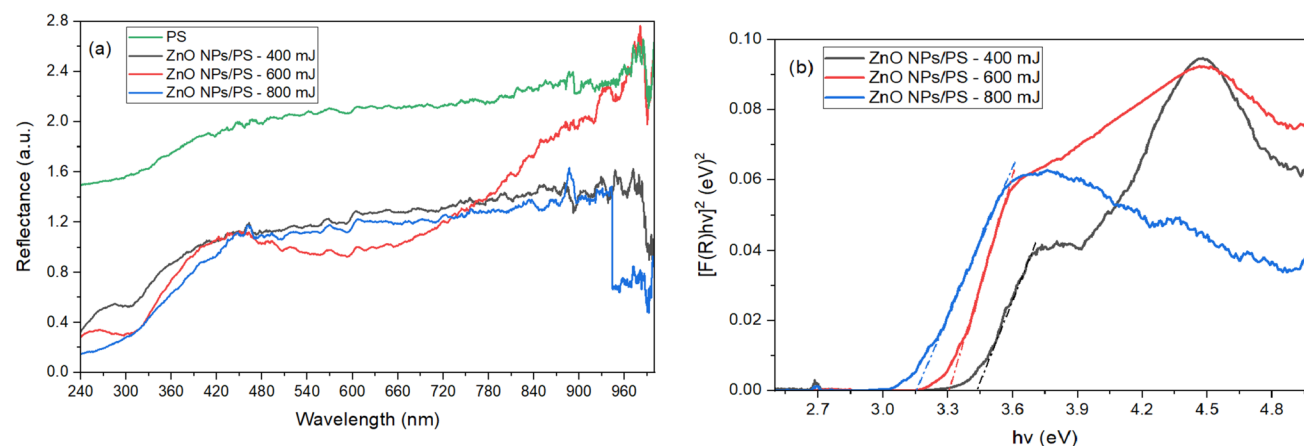
Sample	Number of pulses	Laser energy (mJ)	Absorption peak (nm)	Energy gap (eV)
ZnO	300 shots	400	278.2	3.79
		600	284.7	3.65
		800	291.9	3.44

where A is the constant that depends on the semiconductor properties, α is the expressed absorption coefficient, and $h\nu$ refers to photon energy. Subsequently, the optical band gap of ZnO layer was determined by plotting $(\alpha h\nu)^2$ against photon energy $h\nu$. The extrapolation of a line intersects the photon energy axis at the band gap, as displayed in Fig. 5(b).

Table 2 summarizes the band gap energies of obtained ZnO thin films, which increase from 3.44 to 3.79 eV with increasing laser energy and are higher than the bulk value of 3.37 eV for ZnO [39]. This increase in band gap energy is attributable to the quantum size effect [19]. Based on the results, it can be concluded that the optical band gap energy of the ZnO layer increases as the laser energy used during fabrication is increased.

UV–Vis Diffuse Reflectance Spectroscopy (DRS)

Figure 6 indicates the experimental diffuse reflectance spectra (DRS) for as-prepared porous silicon and ZnO layer deposited on porous silicon using pulse laser deposition with different laser energies in the wavelength range of 240–1000 nm at ambient temperature. Generally, all samples exhibit extremely minimal UV reflectance and a significant rise in the visible and near-IR regions. This

**Fig. 6** **a** Diffuse reflectance spectra of PS and ZnO films PLD technique at various laser energies. **b** Graphical representation of $[F(R)h\nu]^2$ versus the photon energy of ZnO thin films deposited on PS at various laser energies

investigation demonstrated that ZnO thin films deposited on a porous silicon substrate reduce reflectivity. Also, we indicate that the reflectivity rate of the ZnO NPs/PS using the PLD technique at a laser energy of 800 nm decreased at a wavelength of approximately 580 nm and then sharply increased in the near-IR region. The observed change can be related to the fact that the grain size of the film synthesized at 800 nm was higher than that of the prepared samples at 400 and 600 nm, as determined by FE-SEM microscopy. However, we observed that the reflectivity behavior of ZnO NPs/PS using the PLD method at 400 and 600 nm laser energies is almost similar, with a reflection peak observed at approximately 270 nm. The reduction in reflectance is due to forming a roughly ordered structure after filling pores with ZnO NPs. A decrease in reflectance increases the number of photons taken by the detector device, thus enhancing the device's efficiency [40].

Reflectance measurements were transformed into corresponding absorption spectra using the Kubelka–Munk and Tauc relations by the Kubelka–Munk theory [41], as seen in Eqs. (3) and (4) below:

$$F(R) = \frac{\alpha}{S} = \frac{(1-R)^2}{2R} \quad (3)$$

$$F(R) \propto \alpha \propto \frac{A(-h\nu - E_g)^{\frac{1}{2}}}{h\nu} \quad (4)$$

where R represents the reflectance, α denotes the absorption coefficient of ZnO NPs/PS, S indicates the scattering coefficient, and $F(R)$ represents the remission or Kubelka–Munk function. Since the scattering coefficient does not depend on wavelength, $F(R)$ is directly proportional to the absorption coefficient (α).

The band gap for the direct allowed transition of semiconductor absorption is represented by Eq. (4). Therefore, Eq. (4) can be reformulated as

$$[F(R)hv]^2 = A(-hv - E_g) \tag{5}$$

The band gap energy can be calculated from reflectance measurements via plotting $[F(R)hv]^2$ versus the incident photon energy and extrapolating the linear region to the position at which $F(R)$ approaches zero, as illustrated in Fig. 6. The computed band gap (E_g) values for samples synthesized with 400, 600, and 800 mJ laser energies deposited on PS using PLD are 3.45 eV, 3.33, and 3.17 eV, respectively. These values are close to the bulk ZnO energy gap value, demonstrating the great crystallinity of the ZnO layers formed [42].

Photoluminescence (PL) Spectroscopy

A comparison of the photoluminescence emission spectra of porous silicon and ZnO layer deposited on porous silicon at room temperature with different laser energies at an excitation wavelength of 325 nm is presented in Fig. 7. The porous silicon exhibits an extreme PL emission band broadening centered at a visible wavelength of 664.54 nm (1.87 eV), which reveals the excellent quality of the PS structure [43]. This blue shift in porous silicon is the consequence of the radiative recombination of electron–hole pairs induced by photoexcitation and confined within Si nanocrystals. The quantum size effect changes the electronic spectrum due to this confinement [39, 44]. The deposition of ZnO onto the porous silicon surface may influence the size of the silicon crystallites and the surface structure and interface between

ZnO and PS. Moreover, we notice a decrease in the emission of the intense PS peak after the deposition of the porous silicon with ZnO thin film is attributable to the surface oxidation caused by the ZnO layer [45]. However, the red emission regions of the porous silicon and ZnO layer/PS exhibit a red shift with increasing laser energy of the PLD technique. It may be due to nanostructure size and defects at the zinc interface between the ZnO layer and the porous silicon substrate. The FTIR data obtained in this study indicate that the surface of the PS substrate oxidizes after the deposition of the ZnO layer. The PL spectra of ZnO nanostructures exhibit two distinct regions. The first region concerns UV emission caused by the excitonic recombination of the energy state within the band gap associated with free and bound excitons. The second region is related to concentrations of native or intrinsic defect centers in ZnO material, such as zinc vacancy (V_{Zn}), oxygen vacancy (V_o), interstitial zinc (Zn_i), interstitial oxygen (O_i), antisite zinc Zn_{O_i} , and antisite oxygen (O_{Zn}), which cause the visible spectrum [46].

As shown in Fig. 7, we noted four PL emission peaks after coating the PS substrate with the ZnO layer. These peaks are the distinctive emission of the ZnO layer listed in Table 3. The first UV emission peak in the 371–374 nm range can be ascribed to the direct recombination of free excitons at the near band edge [47]. The energy band gap at the wavelength relevant to the UV emission peak agrees closely with the calculated value derived from reflectance and UV–vis spectroscopy. However, the second violet-blue band located at ~443–445 nm comes from the electronic transition from the donor level of Zn_i to the deep holes trapped levels such as V_{Zn} [48]. The next blue band centered at ~487–489 nm relates to the transition between acceptor

Fig. 7 Photoluminescence spectra of PS and ZnO NPs/PS deposited using PLD with different laser energies

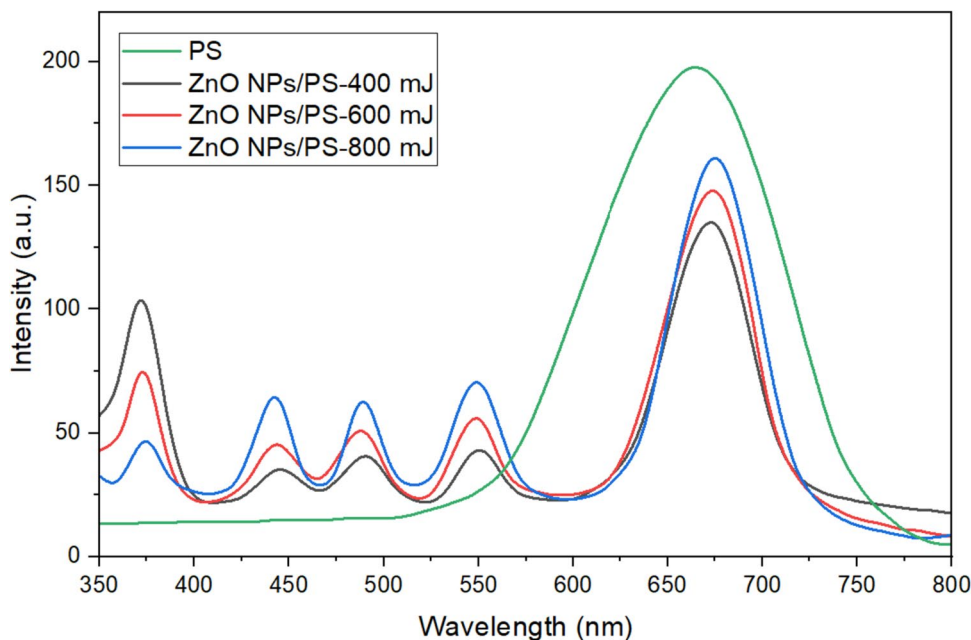


Table 3 PL peak positions of the PS and ZnO NPs/PS

Sample	Laser parameters	Peak positions (nm)	Energy bandgap (eV)
PS	-	664.54	1.87
	400 mJ 300 pulses 1064 nm	371.92	3.33
		445.27	2.78
		490.24	2.53
		550.23	2.25
		672.68	1.84
ZnO NPs/PS	600 mJ 300 pulses 1064 nm	373.14	3.32
		444.13	2.79
		487.96	2.54
		548.82	2.26
		673.65	1.84
	800 mJ 300 pulses 1064 nm	375.09	3.31
		443.58	2.80
		488.92	2.54
		548.43	2.26
		674.87	1.84

and donor levels. The fourth band in the green emission region at ~ 548–550 nm is assigned to the concentration of oxygen vacancies in ZnO film, and the emission originates from the electronic transition from the near conduction band edge to the deep acceptor level [49]. The existence of a green region in the visible spectrum is direct evidence that the ZnO film contains oxygen vacancies or interstitial zinc. In addition, we observed that the PL spectra intensity of UV emission decreases and shows a minor blue shift as laser pulse energy increases of PLD from 400 to 800 mJ during the deposition ZnO layer onto PS.

In contrast, the visible emission intensity decreases. It is attributed to smaller nanostructures having a higher surface-to-volume ratio than bulk material, increasing surface-related luminescence, and the finding indicates that PL peaks are highly responsive to nanostructure size [50]. Hence, the observed increase in UV emission and decrease in defect emission suggest that the ZnO NPs/PS device, which was fabricated using 400 mJ laser energy to deposit a ZnO layer onto the PS substrate, exhibits a higher level of structural perfection compared to other samples.

The findings observed in the energy band gap from reflectance spectra and photoluminescence of ZnO NPs/PS are roughly comparable to those noted from UV–vis spectrum of ZnO thin films deposited on a quartz substrate, as displayed in Table 4. Despite this, the band gap energy computed for

Table 4 Comparison of band gap energies of the ZnO thin films garnered from the UV–vis, PL, and reflectance spectroscopy

Nanostructure type	Laser energy (mJ)	Eg from UV–vis (eV)	E_g from PL (eV)	E_g from reflectance (eV)
		Before deposited Ps	After deposited PS	
ZnO NPs	400	3.79	3.43	3.45
	600	3.65	3.42	3.33
	800	3.44	3.40	3.17

the ZnO layer utilizing reflectance and photoluminescence spectroscopy was equal to or smaller than those estimated with UV–vis spectroscopy. This modest shift in band gap values in ZnO thin films can be attributed to several factors. Besides the effect of laser energy, the substrate type may be one of the most influential factors in the crystalline development of the thin film. These variables may affect the thickness and roughness of the surface, which can improve the optical performance of the detector.

Fourier Transform Infrared Spectroscopy (FTIR Spectrometry)

The FTIR spectrometer supplies an efficient method for detecting the chemical bonds and molecular vibrations present in the prepared sample. The FTIR absorption spectra of both the porous silicon substrate and the zinc oxide layer deposited onto the porous silicon substrate using the PLD process at room temperature with a laser energy of 600 mJ are depicted in Fig. 8. The FTIR spectrum was measured within the mid-IR region at 400–4000 cm^{-1} spectral frequencies. The many types of vibrational modes are described in Table 5. The FTIR spectra in Fig. 8a indicate the presence of bonds arising from diverse functional groups of molecules located on the surface of PS synthesized using a photoelectrochemical approach at a current density of 16 mA/cm^2 and etched for 10 min. The silicon-hydrogen bonds shown in the fabricated PS layers can be identified by the occurrence of the wagging mode of Si–H at a wavenumber of 635.57 cm^{-1} , the Si–H₂ scissor mode noticed at 932.47 cm^{-1} , the stretching mode of Si–H at 2072.28 cm^{-1} , and the Si–H_x mode recorded at 2331.41 cm^{-1} , respectively. In addition, silicon-oxygen bonds were seen at 880.14 cm^{-1} and 1112.55 cm^{-1} , which refer to the Si–O–Si bending and asymmetric stretching modes, respectively. The asymmetric deformation bond of Si–CH₂ was located within the spectral range of 1403.62 cm^{-1} . The intense band at 1633.94 cm^{-1} arose from the scissor bending vibrational of O–H groups, ascribed to the structural hydroxyl group of SiOH and the presence of H₂O bound in the structure. The sharp absorption peak at 2251.20 cm^{-1} was associated with the Si–H stretching mode

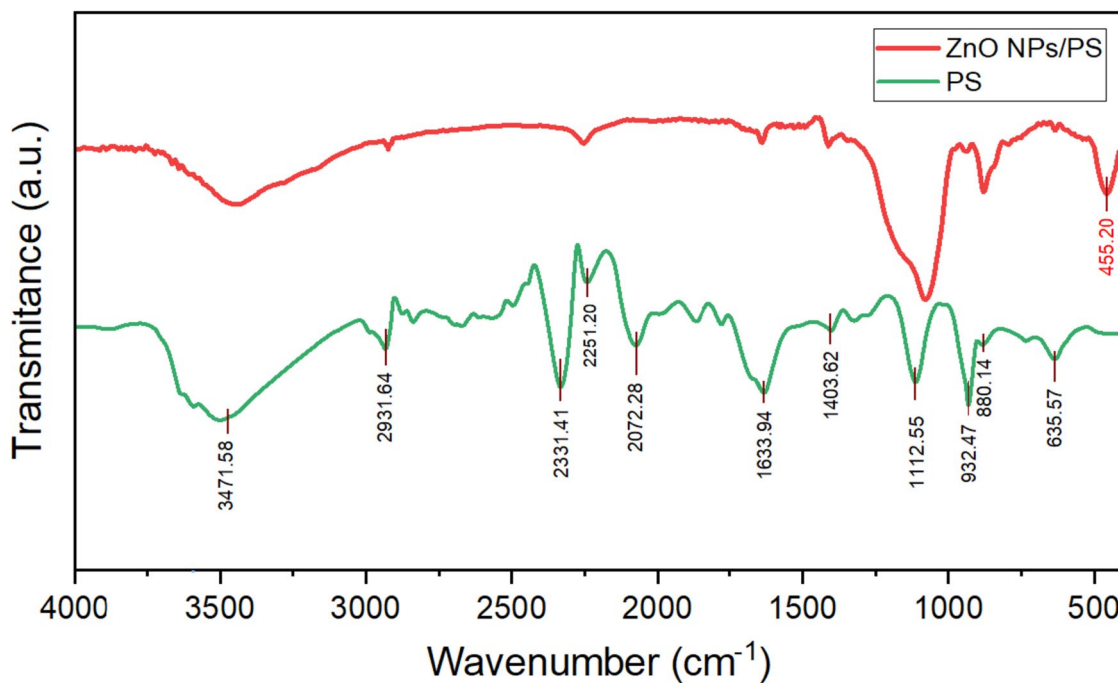


Fig. 8 Typical FTIR spectra of the porous silicon surface and ZnO NPs/PS structure

with three oxygen atoms in back-bonding. The IR peak observed at a wavenumber of 2903.27 cm^{-1} was related to the asymmetric stretching mode of CH_2 . The strong absorption centered at $3000\text{--}3640\text{ cm}^{-1}$ corresponded to the O–H stretching mode of H-bonded SiOH groups. The FTIR peaks match the findings reported in previous studies [51–57]. The FTIR analysis of ZnO NPs/PS varies considerably from that of porous silicon, as represented in Fig. 8. These variations dominate the Si–O and Si–H vibrational modes. An extra

peak centered around 455.2 cm^{-1} was related to the Si–O–Si bend vibrational, as evident in Fig. 8. The intensity of the Si– H_x ($x = 1$ and 2) related peaks at 635.57 cm^{-1} and 932.47 cm^{-1} decreases in the ZnO NPs/PS structure, as illustrated in Fig. 8. In contrast, Si– H_x vibrational bands at 2072.28 cm^{-1} and 2331.41 dissipate from ZnO NPs/PS structure. In addition, the peaks corresponding to the Si–O–Si bridges at 884 cm^{-1} and 1110 cm^{-1} become broader and more significant. The substitution of unstable H-atoms with O- or Zn-atoms is responsible for the increased broadness and amplitude of the Si–O–Si bridges and decreased Si– H_x -related peaks.

Table 5 Identification of the FTIR vibrational frequencies observed in the porous silicon surface and ZnO NPs/PS structure

Wavenumber (cm^{-1})	Bonds	Vibrational modes	Reference
455.20	Zn–O	Stretching	[45]
635.57	Si–H	Wagging	[51]
880.14	Si–O–Si	Bending	[57]
932.47	Si– H_2	Scissor	[56]
1112.55	Si–O–Si	Asymmetric stretching	[52]
1403.62	Si– CH_3	Asymmetric deformation	[55]
1633.94	O–H	Bending	[51]
2072.28	Si–H	Stretching	[52]
2251.20	$\text{O}_3\text{--Si--H}$	Stretching	[53]
2331.41	Si– H_x	-	[52]
2931.64	CH_2	Asymmetric stretching	[52]
3000–3640	Si–OH	Stretching	[54]

Meanwhile, it was stated in research that metal–oxygen–silicon stretches appear below 1000 cm^{-1} , with a large proportion of metal–oxygen bonds oscillating between 400 and 700 cm^{-1} [58]. Consequently, the peak observed in the $400\text{--}700\text{ cm}^{-1}$ range in Fig. 8 can be ascribed to forming a new Zn–O stretching mode through the ZnO NPs/PS structure due to the PS and ZnO interface reaction. The FTIR analysis demonstrates that coating ZnO onto PS leads to surface oxidation, which includes the exchange of instability Si–H modes with more excellent stability Si–O modes when the ZnO NPs/PS system is stored at room temperature and exposed to air [45, 46].

Electrical Measurement

Figure 9(a) shows that the current density–voltage ($J\text{--}V$) curves are obtained using both the forward and reverse

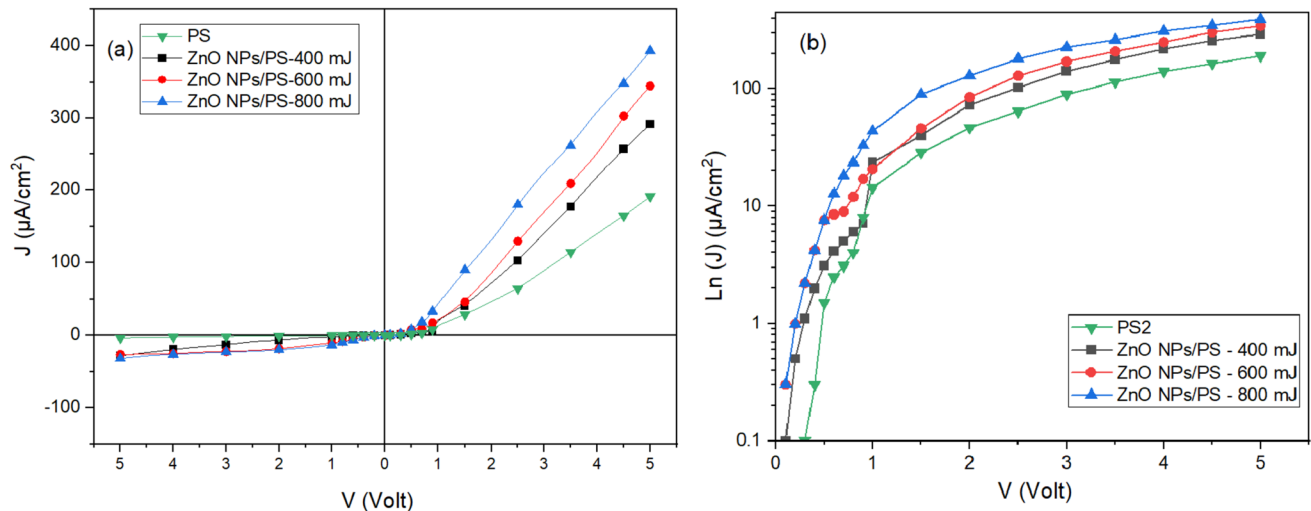


Fig. 9 Current density–voltage curves of the PS/n-Si and ZnONPs/PS/n-Si devices fabricated with different laser energies in the dark case. **a** J - V plot; **b** $\text{Ln}(J)$ - V plot

bias DC voltages between -5 and 5 V. The J - V curves revealed that Al/PS/n-Si/Al and Al/ZnO NPs/PS/n-Si/Al composite devices exhibit rectifying features. This rectifying behavior is caused by a heterojunction potential barrier within the ZnO/PS junction. The energy gap between ZnO and PS is distinct, creating the heterojunction structure.

The J - V curve observations of all structures demonstrate that the current grows exponentially depending on the voltage according to the forward bias case. In contrast, the dark leakage current is minimal in the reverse bias case. The observed rise in current density under the forwarding bias case is attributable to the narrowing the depletion layer at the junctions. Conversely, when the width of the depletion layer expands during reverse bias, the passage of electric charges becomes more constrained, which leads to a reduction in current.

In the forward bias regime, the passing current observed in Al/PS/n-Si/Al structure was less than in Al/ZnONPs/PS/n-Si/Al structures. Because of the large pore size, the PS layer in the device exhibited a high percentage of porosity, resulting in a significant disruption in the PS structure. This caused the PS side of the Si environment less favorable for electron migration. The widening of the band gap in porous silicon can be referred as quantum confinement effects, which also led to a depletion of charge carriers in the porous silicon [19].

The significant characteristics of the heterojunction structures, including the saturation current density (J_s), barrier height (Φ_{Bn}), and ideality factor (n), were obtained using a semilog I - V plot, as shown in Fig. 9(b).

It is possible to determine the saturation current density (J_s) of the dark forward biasing voltage by extrapolating

the current density from the semilog J - V straight part to the zero applied voltage. In addition, the ideality factor (n) can be determined from the slope of the linear portion of the semilog J - V curve employing the following formula [60]:

$$n = \frac{q}{k_B T} \frac{dv}{d(\ln J)} \quad (6)$$

The semilog J - V graphs of PS/n-Si and ZnO/PS/n-Si devices illustrate two distinct slopes corresponding to two different transport mechanisms. The first region exhibits an exponential dependence between passing current and applied voltage, attributed to the recombination mechanism. On the other hand, the second region results from the dominant tunneling mechanism [61]. The ideality factor (n) values were computed using Eq. (8) for the PS/n-Si device and the ZnO/PS/n-Si devices prepared with laser energies of 400, 600, and 800 mJ/pulse, as shown in Fig. 9(b). The calculated ideality factor values were approximately 2.51 for the PS/n-Si device and 2.42, 2.38, and 2.33 for the ZnO/PS/n-Si devices, respectively. We observe that increased laser energy reduces the ideality factor, and diffusion current dominates in the junction. Thus, the heterojunction properties are improved, confirmed by the increased transient current when utilizing higher laser energies. A value of n greater than 2 usually corresponds with one or more factors, like barrier height heterogeneity, significant series resistance in the heterojunctions, interface states, and oxide layer presented in porous silicon surface [26].

The Schottky barrier height (Φ_{Bn}) can be mathematically defined by the following equation [59]:

Table 6 The electrical parameters of the PS/n-Si and ZnONPs/PS/n-Si devices, such as ideality factor values, barrier height, and saturation current density, were evaluated with different laser energies

Type of device	Laser energy (mJ)	J_s ($\mu\text{A}/\text{cm}^2$)	n	Φ_b eV
PS	-	24.122	2.51	0.656
ZnO NPs/PS	400	39.411	2.42	0.643
ZnO NPs/PS	600	51.781	2.38	0.636
ZnO NPs/PS	800	87.563	2.33	0.622

$$\Phi_{Bn} = \frac{k_B T}{q} \ln\left(\frac{A^{**} T^2}{J_s}\right) \tag{7}$$

where J_s is the forward saturation current density ($\mu\text{A}/\text{cm}^2$) and A^{**} (112 for n -type silicon) is the Richardson constant ($\text{A}/\text{K}^2\text{-cm}^2$).

The barrier height for the PS/n-Si device was determined to be 0.65, whereas the ZnO NPs/PS/n-Si devices created via PLD with laser energies of 400, 600, and 800 mJ/pulse had barrier heights of 0.643, 0.636, and 0.622, respectively. Table 6 indicates the electrical features of PS/n-Si and ZnO NPs/PS-n-Si devices fabricated with different laser energies.

Current Density–Voltage (JPh-V) Characteristics Under Illumination

The photocurrent characteristics in reverse biased voltage under white light illumination with different power intensities from 20 to 160 mW/cm^2 at room temperature of Al/ZnO NPs/PS/n-Si/Al device containing ZnO layers deposited at different laser energy are illustrated in Fig. 10.

The photocurrent is observed solely with the reverse biased condition, so light illumination notably enhances the reverse current. As a result, the possibility of electron–hole

separation, depletion region, and the internal electric field significantly increases. Specifically in the depletion layer, light induces the generation of electron–hole pairs.

The photocurrent is proportional to the incident light intensity and increases with reverse bias voltage because electron–hole separation is enhanced. The result is an increase in the number of separated pairs, revealing the promise of the Al/ZnO NPs/PS/n-Si/Al heterojunction as a photodetector.

The photocurrent improved in the ZnO NPs/Ps formed with higher laser energy, which can be ascribed to the enlarging of the depletion region, the extended carrier diffusion length, the decreasing density of the trap state, and the increasing connection between the porous silicon and the zinc oxide nanocrystallites at a laser energy of 800 mJ/pulse.

Photodetector Measurements

Figure 11 depicts the spectral responsivity (R_λ), specific detectivity (D^*), and external quantum efficiency (EQE) of the PS/n-Si and ZnO/PS/n-Si photodetector devices with ZnO layers fabricated on porous silicon substrates using different laser energies. The measurements were conducted over 300 to 900 nm wavelength at a reverse bias of 3 V and room temperature.

The spectral responsivity (R_λ), specific detectivity (D^*), and external quantum efficiency (EQE) are computed via the following formulas [21, 62]:

$$R_\lambda = \frac{I_p}{P_{in}} \tag{8}$$

$$D^* = \frac{\sqrt{A\Delta f}}{NEP} \tag{9}$$

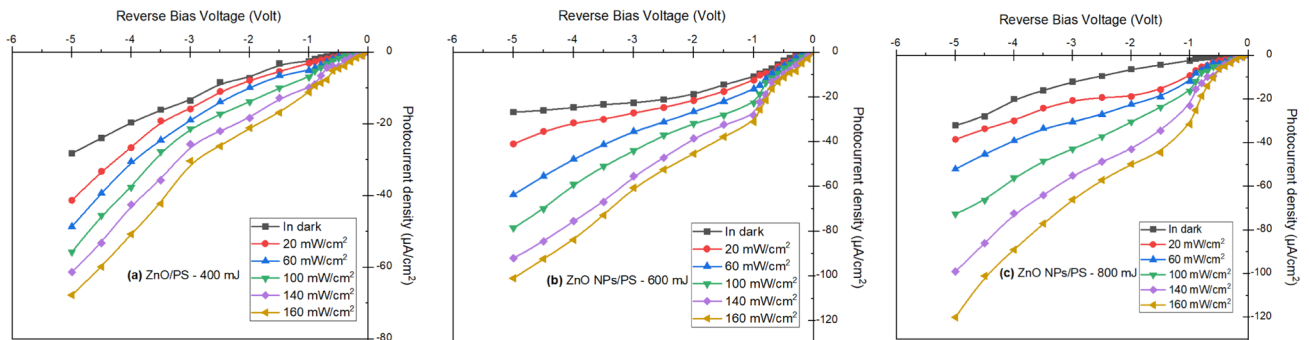


Fig. 10 Photocurrent density curves of Al/ZnO NPs/PS/n-Si/Al de under white light illumination at different laser energies: **a** 400, **b** 600, and **c** 800 mJ

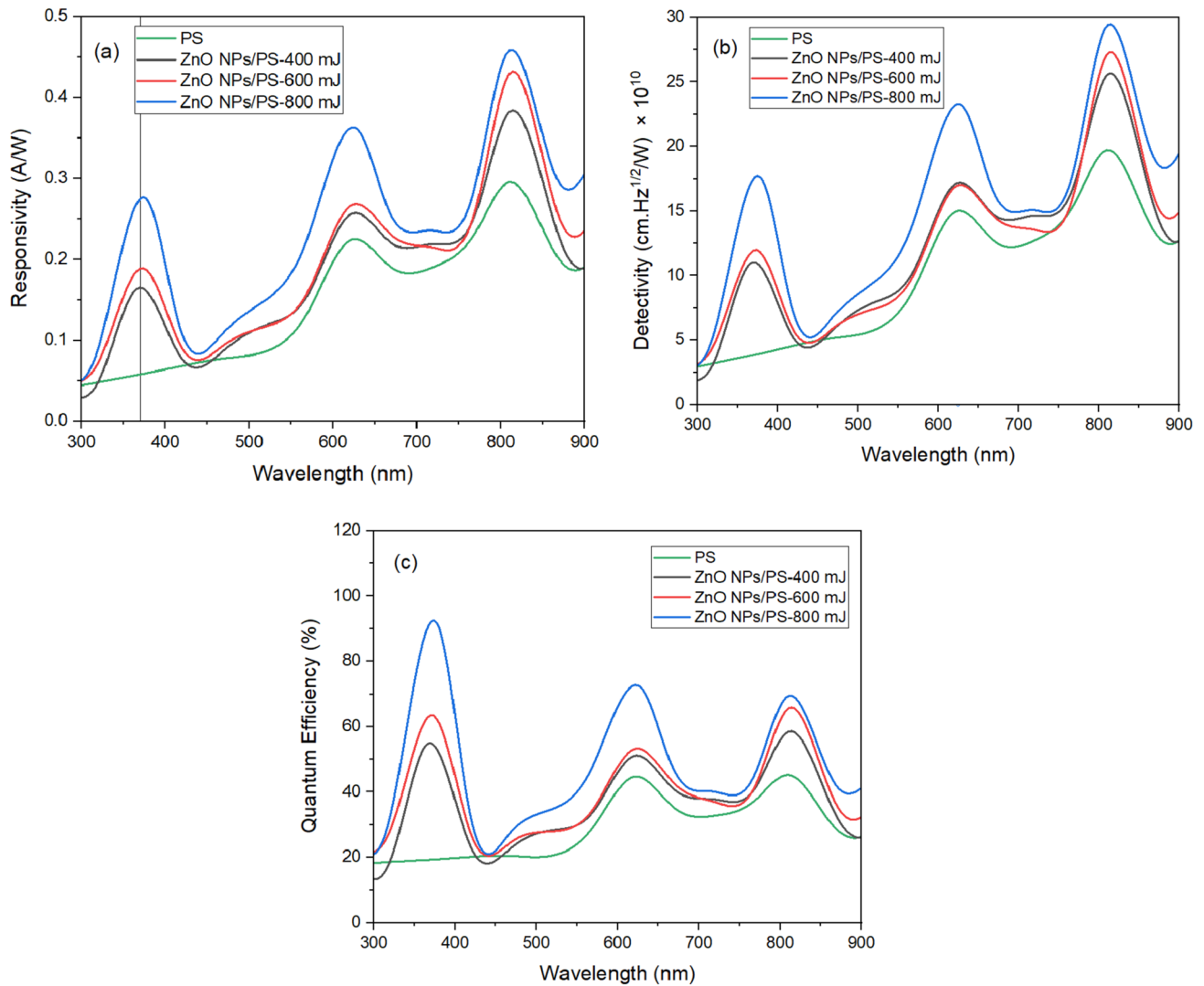


Fig. 11 Curves of merit figures of the of PS/n-Si and ZnO NPs/PS/n-Si photodetectors prepared with different laser energies: **a** the spectral responsivity (R_λ), **b** specific detectivity (D^*), and **c** external quantum

efficiency (EQE) as a function different incident wavelengths ranging from 300 to 900 nm

$$\eta = \frac{h\nu}{q} R_\lambda \quad (10)$$

where P_{in} refers to the incoming optical power, I_p corresponds to the recorded photocurrent, A denotes the area of detector activity, Δf represented bandwidth ($\frac{1}{2\pi\tau}$), ν indicates the frequency of the incident photons, and the term NEP stands for noise equivalent power.

The results indicate that the photodetectors have outstanding spectral responsivity across three broad ranges of wavelengths after the deposition of ZnO thin films, from ultraviolet to near infrared, as shown in Fig. 11(a). ZnO layer is more sensitive to ultraviolet light than to visible or infrared light, which can be assigned to the presence of porous silicon

and silicon, respectively. Figure 11(a) reveals the presence of three distinct spectral responsivity regions in ZnO NPs/PS/n-Si photodetector devices. The first spectral band, centered at ~ 372 nm, represents the ZnO layer's absorption edge. The second spectral zone, located at ~ 632 nm, is ascribed to the porous silicon substrate's absorption edge [63]. The third spectral band observed at ~ 825 nm is due to the silicon content of the manufactured devices.

The spectral responsivity of the ZnO NPs/PS/n-Si device was found to be enhanced by an increase in laser energy. For instance, the spectral responsivity of the device manufactured with 400 mJ of laser energy was discovered to be 0.17 A/W at a wavelength of 370.6 nm, whereas the spectral responsivity of the device manufactured with 800 mJ of laser

energy increased from 0.17 to 0.28 A/W at a wavelength of approximately 374 nm. An insignificant shift in the spectral responsivity curve toward larger wavelengths was observed with increasing laser energy, which can be interpreted as modifications in the energy gap of ZnO thin films. The optimum spectral responsive (R_{λ}), followed at a wavelength of 812.31 nm, was estimated to be approximately 0.46 A/W of ZnO NPs/PS/n-Si device fabricated at 800 mJ laser energy. The improvement in the photodetector's sensitivity can be explained by a variety of characteristics, such as an increase in the depletion width and diffusion length zones, enhanced light absorption, reduced dark current, minimized surface state density, enhanced carriers efficiency, and an improved in absorption surface area (sensitive area) of the photodetector.

The maximal specific detectivity (D^*) was identified to be about 29.48×10^{10} Jones ($\text{cm}\cdot\text{Hz}^{1/2}/\text{W}$) at a wavelength of 812.31 nm of ZnO NPs/PS/n-Si device synthesized at 800 mJ laser energy. The influence of laser energy on the specific detectivity of ZnO NPs/PS/n-Si photodetectors is depicted in Fig. 11(b). It was observed that the specific detectivity graph and the spectral responsivity graph exhibit a similar trend. At a wavelength of ~ 372 nm, the specific detectivity increased from approximately $\sim 11.1 \times 10^{10}$ to $\sim 17.8 \times 10^{10}$ Jones as the laser energy expanded from 400 to 800 mJ. This indicates that the photodetector exhibited a low noise dark current or a high responsivity. The enhancement in the photodetector's detectivity can be associated with an assortment of factors, including a decrease in the concentration of structural imperfections, a reduction in surface states and trapping centers, and a decline in leakage current.

The ZnO NPs/PS/n-Si photodetectors, fabricated using 400, 600, and 800 mJ laser energies, were analyzed to determine their external quantum efficiency (EQE). The results revealed EQE values of 55.38%, 63.87%, and 92.31% at a wavelength of approximately 372 nm, respectively, as illustrated in Fig. 9c. These values are comparable to those reported by Faisal et al. for ZnO/Si photodetectors prepared using the hydrothermal method [64].

Conclusions

In conclusion, this research showed that the morphological, optical, structural, and electrical properties of ZnO layers deposited onto porous silicon substrates by pulsed laser energy were influenced by the laser energy used during the deposition process. The X-ray diffraction analyses reveal that the ZnO phase exhibits a polycrystalline nature, characterized by a hexagonal wurtzite structure. In addition, there is evidence of a preferred orientation along the (002) plane.

The ZnO layer formed on porous silicon has characteristic photoluminescence emission peaks extending from the ultraviolet to the visible spectrum. An observed result was a

decline in the optical energy gap of the manufactured samples when the laser energy was increased. The measured values of the optical energy gap ranged from 3.44 to 3.79 eV. The photocurrent improved in the ZnONPs/Ps formed with higher laser energy. The FTIR analysis shows that an instability Si–H modes exchange with more excellent stability Si–O modes or Zn–O stretching when the porous silicon is coated with the ZnO layer.

The electrical properties revealed that the flow current Al/ZnO NPs/PS/n-Si/Al structures are higher than Al/PS/n-Si/Al structure in the dark forward bias case. The utilization of porous silicon as a substrate for depositing ZnO thin films has been demonstrated to enhance the light trapping and absorption characteristics. This enhancement consequently results in an improved spectral responsivity of ZnO NPS/PS/n-Si photodetectors. The ZnONPs/PS/n-Si photoreactor fabricated at a laser energy of 800 mJ/pulse has the lowest ideal factor of 2.33 and the most prominent external quantum efficiency (EQE) in the UV region of 92.31%.

Acknowledgements The authors would like to thank the University of Technology-Iraq for the logistic support of this work.

Author Contribution Ali J. Hadi—writing original draft, methodology, investigation, and formal analysis. Uday M. Nayef, Falah A.-H. Mutlak, and Majid S. Jabir—main concept, data interpretation, and supervision. Uday M. Nayef—writing—review and editing, visualization, and data curation.

Data Availability No applicable.

Declarations

Conflict of Interest The authors declare no competing interests.

References

1. Nayef UM, Hadi AJ, Abdulridha SK, Mutlak FAH, Ahmed AF (2022) Tin dioxide nanoparticles synthesized via laser ablation in various liquids medium. *J Opt (India)*. <https://doi.org/10.1007/s12596-022-00913-0>
2. Mutlak FA-H, Ahmed AF, Nayef UM, Al-zaidi Q, Abdulridha SK (2021) Improvement of absorption light of laser texturing on silicon surface for optoelectronic application. *Optik* 237:166755. <https://doi.org/10.1016/j.ijleo.2021.166755>
3. Mahmood RI, Kadhim AA, Ibraheem S, Albukhaty S, Mohammed-Salih HS, Abbas RH, Al-Karagoly H (2022) Biosynthesis of copper oxide nanoparticles mediated *Annona muricata* as cytotoxic and apoptosis inducer factor in breast cancer cell lines. *Sci Rep* 12(1). <https://doi.org/10.1038/s41598-022-20360-y>
4. Aryanto D, Jannah WN, Masturi Sudiro T, Wismogroho AS, Sebayang P, Marwoto P (2017) Preparation and structural characterization of ZnO thin films by sol-gel method. In *Journal of Physics: Conference Series* (Vol. 817). Institute of Physics Publishing. <https://doi.org/10.1088/1742-6596/817/1/012025>
5. Hadi AJ, Nayef UM, Jabir MS, Mutlak FA-H (2023) Synthesis of vanadium pentoxide nanoparticles via laser ablation for biomedical applications. *Int J Mod Phys B*. <https://doi.org/10.1142/S0217979224502308>

6. Kumar R, Kumar G, Umar A (2014) Zinc oxide nanomaterials for photocatalytic degradation of methyl orange: a review. *Nanosci Nanotechnol Lett* 6(8):631–650. <https://doi.org/10.1166/nml.2014.1879>
7. Jabir MS, Rashid TM, Nayef UM, Albukhaty S, Almalki FA, Albaqami J, Sulaiman GM (2022) Inhibition of *Staphylococcus aureus* α -hemolysin production using nanocurcumin capped Au@ZnO nanocomposite. *Bioinorg Chem Appl*. <https://doi.org/10.1155/2022/2663812>
8. Khudiar SS, Mutlak FA-H, Nayef UM (2021) Synthesis of ZnO nanostructures by hydrothermal method deposited on porous silicon for photo-conversion application. *Optik* 247:167903. <https://doi.org/10.1016/j.ijleo.2021.167903>
9. Ningsih SKW, Nizar UK, Bahrizal Nasra E, Suci RF (2019) Effect of egg white as additive for synthesis and characterization of Al doped ZNO nanoparticles by using sol-gel method. *J Phys Conf Ser* 1185(1). <https://doi.org/10.1088/1742-6596/1185/1/012029>
10. Ngom BD, Mpahane T, Manyala N, Nemraoui O, Buttner U (2009) Applied Surface Science Structural and optical properties of nano-structured tungsten-doped ZnO thin films grown by pulsed laser deposition 255:4153–4158. <https://doi.org/10.1016/j.apsusc.2008.10.122>
11. A HC, Shen H, Yin Y, Lu L, Shen J, Tang Z (2009) The effects of porous silicon on the crystalline properties of ZnO thin films. *J Phys Chem Solids* 70(6):967–971. <https://doi.org/10.1016/j.jpcc.2009.05.004>
12. Abed MA, Mutlak FAH, Ahmed AF, Nayef UM, Abdulridha SK, Jabir MS (2021) Synthesis of Ag/Au (core/shell) nanoparticles by laser ablation in liquid and study of their toxicity on blood human components. *J Phys Conf Ser* 1795(1). <https://doi.org/10.1088/1742-6596/1795/1/012013>
13. Ryu YR, Zhu S, Budai JD, Chandrasekhar HR, Miceli PF, White HW (2013) Optical and structural properties of ZnO films deposited on GaAs by pulsed laser deposition optical and structural properties of ZnO films deposited on GaAs by pulsed laser deposition 201(2000). <https://doi.org/10.1063/1.373643>
14. Tsoutsouva MG, Panagopoulos CN, Papadimitriou D, Fasaki I, Kompitsas M (2011) ZnO thin films prepared by pulsed laser deposition. *Mater Sci Eng, B* 176(6):480–483. <https://doi.org/10.1016/j.mseb.2010.03.059>
15. He J, Tan B, Wei Q, Su Y, Yang S (2012) Growth and characterization of ZnO thin films grown by pulsed laser deposition 390:6289–6292. <https://doi.org/10.4028/www.scientific.net/AMR.383-390.6289>
16. Hassan D, Zayer M (2021) Study and investigation of the effects of the OTA technique on the physical properties of the ZnO thin films prepared by PLD. *J Appl Sci Nanotechnol* 1(4):32–43. <https://doi.org/10.53293/jasn.2021.3805.1045>
17. Wisz G, Virt I, Sagan P, Potera P, Yavorskyi R (2017) Structural, optical and electrical properties of zinc oxide layers produced by pulsed laser deposition method. *Nanoscale Res Lett* 12(1). <https://doi.org/10.1186/s11671-017-2033-9>
18. Dariani RS, Zabihipour M (2016) Effect of electrical behavior of ZnO microparticles grown on porous silicon substrate. *Appl Phys A: Mater Sci Process* 122(12). <https://doi.org/10.1007/s00339-016-0516-7>
19. Muhsin Nayef U, Waleed Muayad M, Amer Khalaf H (2014) ZnO/PS/p-Si heterojunction properties. *EPJ Applied Physics* 66(2):1–5. <https://doi.org/10.1051/epjap/2014130470>
20. Suliman E, Nayef U, Mutlak F (2022) Synthesis of Au:TiO₂ nanoparticles via laser ablation in liquid deposited on porous-Si for improved spectral responsivity. *J Appl Sci Nanotechnol* 2(3):147–156. <https://doi.org/10.53293/jasn.2022.4558.1125>
21. Nayef UM, Khalaf HA (2017) Optimization photodetectors from zinc sulfide deposited on porous silicon with different doping metals. *Surf Rev Lett* 24(6). <https://doi.org/10.1142/S0218625X1750086X>
22. Gao K, Zhang W, Sun J, Xu N, Ying ZF, Li Q, Wu JD (2009) Influences of substrate and annealing on the structural and optical properties and photoluminescence of nanocrystalline ZnO films prepared by plasma assisted pulsed laser deposition 3(100):19139–19144
23. Wang CF, Hu B, Yi HH (2012) The study of structure and optoelectronic properties of ZnS and ZnO films on porous silicon substrates. *Optik* 123(12):1040–1043. <https://doi.org/10.1016/j.ijleo.2011.07.027>
24. Abood MK, Fayad MA, Al Salihi HA, Salbi HAA (2021) Effect of ZnO nanoparticles deposition on porous silicon solar cell. *Materials Today: Proceedings*, vol 42. Elsevier Ltd, pp 2935–2940. <https://doi.org/10.1016/j.matpr.2020.12.771>
25. Abed SM, Mohammad SM, Hassan Z, Muhammad A, Rajamanickam S, Ali K (2022) Comparative study of UV-ZnO NRs photodetectors based on seeded porous silicon by RF-sputtering and drop-casting methods. *J Mater Sci: Mater Electron* 33(35):26322–26342. <https://doi.org/10.1007/s10854-022-09315-1>
26. Çetinel A, Utlu G (2023) Preparation and characterization of electrochemically deposited Cu₂O/ZnO heterojunctions on porous silicon. *ACS Omega* 8(23):20801–20809. <https://doi.org/10.1021/acsomega.3c01438>
27. Jwied DH, Nayef UM, Mutlak FAH (2021) Synthesis of C:Se nanoparticles ablated on porous silicon for sensing NO₂ and NH₃ gases. *Optik* 241(March). <https://doi.org/10.1016/j.ijleo.2021.167013>
28. Hadi AJ, Nayef UM, Jabir MS, Mutlak FAH (2023) Laser-ablated tin dioxide nanoparticle synthesis for enhanced biomedical applications. *Plasmonics* (0123456789). <https://doi.org/10.1007/s11468-023-01888-9>
29. Razali NSM, Rahim AFA, Radzali R, Mahmood A, Yusuf Y, Zulkifli F, Bakar AA (2019) Investigation on the effect of direct current and integrated pulsed electrochemical etching of N-type (100) silicon. *Acta Physica Polonica A* 135(4):697–701. <https://doi.org/10.12693/APhysPolA.135.697>
30. Razi F, Rahimi F, Irajizad A (2008) Fourier transform infrared spectroscopy and scanning tunneling spectroscopy of porous silicon in the presence of methanol. *Sens Actuators, B Chem* 132(1):40–44. <https://doi.org/10.1016/j.snb.2008.01.032>
31. Khudiar S, Nayef U, Mutlak F (2022) Preparation and characterization of porous silicon for photodetector applications. *J Appl Sci Nanotechnol* 2(2):64–69. <https://doi.org/10.53293/jasn.2021.3646.1032>
32. Tsoutsouva MG, Panagopoulos CN, Kompitsas M (2011) Laser energy density, structure and properties of pulsed-laser deposited zinc oxide films. *Appl Surf Sci* 257(14):6314–6319. <https://doi.org/10.1016/j.apsusc.2011.02.073>
33. Zhu BL, Zhao XZ, Su FH, Li GH, Wu XG, Wu J, Liu J (2007) Structural and optical properties of ZnO thin films on glass substrate grown by laser-ablating Zn target in oxygen atmosphere. *Physica B: Condensed Matter* 396(1–2):95–101. <https://doi.org/10.1016/j.physb.2007.03.018>
34. Ansari AR, Hussain S, Imran M, Al-Ghamdi AA, Chandan MR (2018) Optical investigations of microwave induced synthesis of zinc oxide thin-film. *Materials Science- Poland* 36(2):304–309. <https://doi.org/10.1515/msp-2018-0041>
35. Zare M, Keerthiraj N, Hezam A, Drmsh Q (2019) Novel green biomimetic approach for synthesis of ZnO-Ag nanocomposite; antimicrobial activity against food-borne pathogen, biocompatibility and solar photocatalysis optimization of the surface roughness in ball end milling of titanium alloy Ti-6Al-4V using the Taguchi Method View project International Medical Graduate Guide to the Neurosurgery Match. The Neurosurgical Atlas, by Aaron Cohen-Gadol, M.D. View project. <https://doi.org/10.1038/s41598-019-44309>

36. Venkatachalam S, Kanno Y (2009) Preparation and characterization of nano and microcrystalline ZnO thin films by PLD. *Curr Appl Phys* 9(6):1232–1236. <https://doi.org/10.1016/j.cap.2009.02.003>
37. Hadi AJ, Nayef UM, Mutlak FAH, Jabir MS (2023) Laser-ablated zinc oxide nanoparticles and evaluation of their antibacterial and anticancer activity against an ovarian cancer cell line: in vitro study. *Plasmonics*. <https://doi.org/10.1007/s11468-023-01933-7>
38. Hadi AJ, Nayef UM, Jabir MS, Mutlak FA-H (2023) Titanium dioxide nanoparticles prepared via laser ablation: evaluation of their antibacterial and anticancer activity. *Surf Rev Lett*. <https://doi.org/10.1142/S0218625X2350066X>
39. Nayef UM, Muayad MW, Khalaf HA (2014) Effect of ZnO layers on porous silicon properties. *Int J Electrochem Sci* 9(5):2278–2284
40. Yamlahi Alami Z, Salem M, Gaidi M, El Khamkhami J (2018) Structural, optical and electrical characterizations of ZnO/PS. In *MATEC Web of Conferences*, vol 191. EDP Sciences. <https://doi.org/10.1051/mateconf/201819100013>
41. Mishra V, Warshi MK, Sati A, Kumar A, Mishra V, Sagdeo A, Sagdeo PR (2018) Diffuse reflectance spectroscopy: an effective tool to probe the defect states in wide band gap semiconducting materials. *Mater Sci Semicond Process* 86:151–156. <https://doi.org/10.1016/j.mssp.2018.06.025>
42. Pavlenko M, Myndrul V, Gottardi G, Coy E, Jancelewicz M, Iatsunskiy I (2020) Porous silicon-zinc oxide nanocomposites prepared by atomic layer deposition for biophotonic applications. *Materials* 13(8). <https://doi.org/10.3390/MA13081987>
43. Nayef UM, Khudhair IM (2017) Study of porous silicon humidity sensor vapors by photoluminescence quenching for organic solvents. *Optik* 135:169–173. <https://doi.org/10.1016/j.ijleo.2017.01.060>
44. Cetinel A, Artunç N, Sahin G, Tarhan E (2015) Influence of applied current density on the nanostructural and light emitting properties of n-type porous silicon. *Int J Mod Phys B* 29(15):1–15. <https://doi.org/10.1142/S0217979215500939>
45. Kayahan E (2010) White light luminescence from annealed thin ZnO deposited porous silicon. *J Lumin* 130(7):1295–1299. <https://doi.org/10.1016/j.jlumin.2010.02.042>
46. Chen W, Yao C, Gan J, Jiang K, Hu Z, Lin J, Wu J (2020) ZnO colloids and ZnO nanoparticles synthesized by pulsed laser ablation of zinc powders in water. *Mater Sci Semicond Process* 109:104918. <https://doi.org/10.1016/j.mssp.2020.104918>
47. Liu ZW, Ong CK, Yu T, Shen ZX (2006) Catalyst-free pulsed-laser-deposited ZnO nanorods and their room-temperature photoluminescence properties. *Appl Phys Lett* 88(5):1–3. <https://doi.org/10.1063/1.2168675>
48. Wei X, Zhao R, Shao M, Xu X, Huang J (2013) Fabrication and properties of ZnO/GaN heterostructure nanocolumnar thin film on Si (111) substrate. *Nanoscale Res Lett* 8(1):1–7. <https://doi.org/10.1186/1556-276X-8-112>
49. Ridhuan NS, Abdul Razak K, Lockman Z, Abdul Aziz A (2012) Structural and morphology of ZnO nanorods synthesized using ZnO seeded growth hydrothermal method and its properties as UV sensing. *PLoS one* 7(11). <https://doi.org/10.1371/journal.pone.0050405>
50. Dorrani D, Eskandari AF (2015) Effect of laser fluence on the characteristics of ZnO nanoparticles produced by laser ablation in acetone. *Mol Cryst Liq Cryst* 607(1):1–12. <https://doi.org/10.1080/15421406.2014.927414>
51. Khalifa M, Hajji M, Ezzaouia H (2012) Purification of silicon powder by the formation of thin porous layer followed by photo-thermal annealing. *Nanoscale Res Lett* 7. <https://doi.org/10.1186/1556-276X-7-444>
52. Vázquez-A MA, Aguila Rodríguez G, García-Salgado G, Romero-Paredes G, Peña-Sierra R (2007) FTIR and photoluminescence studies of porous silicon layers oxidized in controlled water vapor conditions. *Revista Mexicana de Física*, vol 53. Retrieved from <http://www.redalyc.org/articulo.oa?id=57053601>
53. Juarez MF, Patrio EM, Paredes-Olivera P (2009) Quantum mechanical investigation of the influence of the local environment on the vibrational properties of hydrogenated Si(111). *J Phys Chem C* 113(2):681–690. <https://doi.org/10.1021/jp808104f>
54. Rocchia M, Garrone E, Geobaldo F, Boarino L, Sailor MJ (2003) Sensing CO₂ in a chemically modified porous silicon film. *Physica Status Solidi (A) Applied Research*, vol 197. pp 365–369. <https://doi.org/10.1002/pssa.200306526>
55. Nayef UM, Hussein HT, Abdul Hussien AM (2018) Study of photoluminescence quenching in porous silicon layers that using for chemical solvents vapor sensor. *Optik* 172:1134–1139. <https://doi.org/10.1016/j.ijleo.2018.07.112>
56. Nayef UM, Khudhair IM (2018) Synthesis of gold nanoparticles chemically doped with porous silicon for organic vapor sensor by using photoluminescence. *Optik* 154:398–404. <https://doi.org/10.1016/j.ijleo.2017.10.061>
57. Ngamou PHT, Overbeek JP, Kreiter R, Van Veen HM, Vente JF, Wienk IM, Creatore M (2013) Plasma-deposited hybrid silica membranes with a controlled retention of organic bridges. *J Mater Chem A* 1(18):5567–5576. <https://doi.org/10.1039/c3ta00120b>
58. Parler CM, Ritter JA, Amiridis MD (n.d.) Infrared spectroscopic study of sol-gel derived mixed-metal oxides. Retrieved from www.elsevier.com/locate/jnoncrysol
59. Das M, Sarmah S, Barman D, Sarma BK, Sarkar D (2020) Distinct band UV-visible photo sensing property of ZnO-porous silicon (PS):p-Si hybrid MSM heterostructure. *Mater Sci Semicond Process* 118. <https://doi.org/10.1016/j.mssp.2020.105188>
60. Jwied DH, Nayef UM, Mutlak FAH (2021) Preparation and characterization of C: Se nano-rods ablated on porous silicon. *Optik* 239:166811. <https://doi.org/10.1016/j.ijleo.2021.166811>
61. Ismail RA, Habubi NF, Ali AM (2012) Structural and electrical properties of CdO/porous-Si heterojunction. *Iraqi J Phys* 10.
62. Jwar AJ, Nayef UM, Mutlak FAH (2023) Study effect of magnetic field on Au-TiO₂ core-shell nanoparticles via laser ablation deposited on porous silicon for photodetector. *Plasmonics* 595–605. <https://doi.org/10.1007/s11468-023-01791-3>
63. Abdulkhaleq NA, Hasan AK, Nayef UM (2020) Enhancement of photodetectors devices for silicon nanostructure from study effect of etching time by photoelectrochemical etching technique. *Optik* 206:164325. <https://doi.org/10.1016/j.ijleo.2020.164325>
64. Faisal AD, Ismail RA, Khalef WK, Salim ET (2020) Synthesis of ZnO nanorods on a silicon substrate via hydrothermal route for optoelectronic applications. *Opt Quantum Electron* 52(4):1. <https://doi.org/10.1007/s11082-020-02329-1>

Publisher's Note Springer Nature remains neutral with regard to jurisdictional claims in published maps and institutional affiliations.

Springer Nature or its licensor (e.g. a society or other partner) holds exclusive rights to this article under a publishing agreement with the author(s) or other rightsholder(s); author self-archiving of the accepted manuscript version of this article is solely governed by the terms of such publishing agreement and applicable law.